

## Dynamic field testing of a 15-year-old friction pendulum base-isolated residential building

P.M. Calvi <sup>\*</sup> , A. Rapone, T.C. Becker, H. Sucuoglu , G. Gabbianelli , B. Chalarca , I. Lanese , G.J. O'Reilly, E. Rizzo-Parisi, F. Dacarro

### ABSTRACT

This paper presents a landmark full-scale experimental program aimed at advancing the understanding of long-term performance of seismic base isolation for buildings in real service conditions. A three-story residential structure in Arischia (L'Aquila, Italy), base-isolated with Friction Pendulum (FP) bearings in service for over 15 years, was subjected to in-situ dynamic testing. Using custom-designed self-reacting frames and the EUCENTRE's mobile laboratory, displacement-controlled sinusoidal loading histories were applied, covering a range of amplitudes and peak velocities. This paper details the test specimen, experimental setup, loading protocols, and instrumentation. It presents preliminary findings on key isolation system properties, including post-elastic stiffness, static and dynamic friction coefficients, and equivalent damping ratio. These results provide rare field-based insight into the effects of aging on FP isolators and offer critical validation data for models used in performance-based assessment of base-isolated structures. In addition, the study demonstrates the feasibility and value of in-situ testing, which can serve as a model for future full-scale investigations of base-isolated buildings.

### 1. Introduction

Seismic isolation is one of the most effective strategies for enhancing the seismic performance of buildings, offering protection to both structural and non-structural components. Over the years, various types of isolation bearings have been developed, but elastomeric and sliding bearings remain the two most widely adopted systems in practice.

Design procedures, assessment methodologies, and modeling strategies for base-isolated structures are well-established and included in all major seismic design codes. Both elastomeric and sliding bearings have been widely implemented for buildings, bridges, and other infrastructure (e.g., Ref. [1,2]). However, the current understanding of isolation behavior is largely based on component-level tests of new bearings (e.g., Ref. [3–9]) or on numerical analysis (e.g., Ref. [10–14]), with limited insight into the performance of systems comprising large numbers of isolators. In a system, each isolator potentially exhibits slight variations in mechanical properties within acceptable tolerances. Moreover, interaction between the isolation layer and the substructure or superstructure can influence bearing demands in complex ways. For instance, torsional coupling between the superstructure and the isolation system can lead to uneven load distribution among the bearings, increasing the demand on some units while reducing it on others [15]. Similarly, flexibility or rocking of the substructure can amplify horizontal displacements at the isolation level, potentially altering the effective stiffness and energy dissipation characteristics of the system

[16–18].

Long-term, system performance is further complicated by material aging and environmental exposure, which may cause significant deviations from the original design behavior [19]. For elastomeric bearings, aging manifests through oxidation, which leads to degradation in mechanical properties, and rubber crystallization from cold exposure, which can increase both horizontal and vertical stiffness [20,21]. Sliding bearings also exhibit non-trivial changes over time: friction coefficients may rise due to material creep and increased contact area, while environmental contamination from moisture or debris can significantly alter their behavior [22,23].

Although some experimental efforts have focused on aged bearings, they remain sparse. Hamaguchi et al. [24] and Van Engelen and Kelly [25] reported on elastomeric bearings aged in service or in storage, revealing changes in stiffness and creep behavior. Other studies have employed accelerated aging methods or examined fatigue in bridge bearings (e.g., Ref. [26]). In contrast, publicly available test data on aged sliding bearings is extremely limited, with Alvarado and Ryan [23] being a rare exception.

To address aging effects in design, current codes introduce empirical modification factors to account for long-term degradation and temperature sensitivity (e.g., Ref. [27]; EC8, 2005). However, these are largely informed by small-scale or component-level data. Full-scale tests, such as those conducted at UC San Diego or E-Defense (e.g., Ref. [28–30]) and elsewhere (e.g., Ref. [31,32]), have relied on new isolation devices.

\* Corresponding author.

E-mail address: [pmc85@uw.edu](mailto:pmc85@uw.edu) (P.M. Calvi).

Similarly, in-situ experiments to date have focused on recently installed systems and have primarily involved simplified loading protocols such as snap-back or free-vibration tests (e.g., Ref. [33–35]); hence, the in-situ effects of aging remain a largely unaddressed issue.

Clearly, further research is needed to assess the impact of aging and system-level variability on the seismic performance of base-isolated structures [36]. This critical gap in knowledge motivated the PASFIT (Performance Assessment of Sliding and Elastomeric Base Isolation Technologies) project.

At the core of PASFIT is the in-situ testing of a real, full-scale three-story residential building in Arischia (L'Aquila, Italy), base isolated using a Friction Pendulum System (FPS) comprising 32 devices. This structure has been in continuous service for over 15 years, making it an ideal case study for investigating the long-term behavior of isolation systems under actual environmental and operational conditions. The project aims to fill critical knowledge gaps regarding how aging, degradation, and inter-unit variability, influence the FPS.

This work complements and builds upon ongoing research at the EUCENTRE Foundation, focused on testing individual isolators from the same building stock. By integrating system-level field test results with component-level data, PASFIT offers a rare opportunity to collect data that can be used to directly validate analytical models and refine assumptions typically used in base isolation design and performance assessment. Moreover, this project addresses pressing local concerns related to the seismic safety of base-isolated buildings in the L'Aquila region, potentially guiding future risk mitigation strategies and policy interventions.

The field testing presented herein involved over 20 controlled experiments and was conducted using the EUCENTRE's state-of-the-art mobile laboratory (MOBILAB) [37] alongside custom-built self-reacting steel frames deployed on-site. The experimental setup was designed to characterize base isolation parameters such as post-activation stiffness, the sliding surface's friction coefficient, and energy dissipation capacity under multi-cycle sine wave loadings at prescribed displacement amplitudes. While most of the tests were focused on generating reliable data within the operating limits of the setup, a subset was intended to explore the performance boundaries of the mobile laboratory. These exploratory tests involved loading conditions beyond the nominal control capabilities of the system, which led to instability in force tracking and overall control performance, thereby compromising the reliability of the results. Therefore, only the 12 tests that fall within the demonstrated reliability of the experimental setup are analyzed and discussed in this paper. However, all raw data (including that from the exploratory tests) are made available for interested readers [38]. This paper presents the key aspects of the experimental program, including a detailed description of the case study building, testing equipment, loading protocols, and instrumentation. Preliminary results are summarized, with emphasis on the evolution of frictional and stiffness characteristics as inferred from the field data. These findings not only highlight the importance of considering aging in performance-based isolation design but also demonstrate the feasibility and value of in-situ testing for advancing seismic protection technologies.

## 2. Case study structure

### 2.1. C.A.S.E. project buildings

Following the 2009 L'Aquila earthquake, 185 base-isolated buildings were constructed across 20 locations in the vicinity of L'Aquila, Italy, as part of the C.A.S.E. (Complessi Antisismici Sostenibili ed Ecocompatibili) Project [1,39]. This initiative aimed to provide safe, seismically resilient housing for approximately 12,000 people displaced by the disaster. A typical C.A.S.E. building comprises a three-story superstructure supported by a 20 m × 60 m, 500 mm thick reinforced concrete slab. This slab is elevated on 40 seismic isolation bearings (although

32-bearing configurations were also implemented), which rest atop circular hollow steel section (HSS) columns. The columns are arranged in a 6 m × 6 m grid and anchored to a 500 mm thick reinforced concrete foundation that interfaces directly with the ground.

The buildings were constructed using various structural materials, resulting in a total of 92 timber, 57 reinforced concrete, and 36 steel-framed structures. This difference in construction materials for the superstructure was adopted to allow a faster reconstruction effort by mobilizing different sectors simultaneously, but it is underlined that all buildings possessed the same substructure typology separated by an isolation layer. The total weight of the superstructures varied slightly and typically ranges between 30 and 40 MN, corresponding to an average axial load of approximately 1 MN per column. The fundamental period of vibration for the non-isolated superstructures typically falls between 0.25 s and 0.45 s. Two primary isolation systems were employed: one configuration includes 12 elastomeric isolators combined with 28 multidirectional sliding pot bearings, while the other consists of 40 Friction Pendulum bearings. The elastomeric system allows for maximum horizontal displacements of up to 360 mm, whereas the FP system accommodates displacements up to 260 mm.

The case study structure designated "Building 20.4" was chosen from among the currently unoccupied buildings based on its compatibility with the available experimental equipment and its representative physical characteristics, such as mass and geometry with respect to all buildings constructed. Building 20.4 (see Fig. 1) is one of four structures located in Arischia, a small village near L'Aquila, Italy.

### 2.2. Case-study building properties

Building 20.4, shown in Fig. 2, is a residential three-story timber structure comprising three interconnected wings linked by two stair-elevator units and accommodating six apartments per floor. The two side wings have plan dimensions of 12 m × 6 m, while the central wing is four times larger, with dimensions 12 m × 24 m. The story heights range between 3.13 m and 3.20 m, while the loft space has a maximum height of approximately 2.5 m. The total building height, from the top of the reinforced concrete slab supporting the superstructure to the ridge of the pitched roof, measures approximately 12 m. The entire structure rests on a 500 mm thick, 21 m × 45 m reinforced concrete slab, which sits on 32–2.45 m tall, hollow steel columns with outer diameter of 800 mm. Plan and elevation views along with other key dimensions are provided in Figs. 3 and 4.

The structural mass of the timber building alone is approximately 600 tonnes. When combined with the concrete slab, the total dead mass reaches about 1500 tonnes, excluding live loads. The building alone has an estimated fundamental period of vibration of 0.26 s and was designed for a base shear of  $0.2W$ , where  $W$  is the weight of the building. Note that Building 20.4, which is about 20 % smaller (in dimensions) than the average C.A.S.E. building, was preferred over its larger companions for its lower mass and overall dimensions. This granted more testing flexibility during the experimental program (e.g., higher testing displacement, velocity, and acceleration).

The building is equipped with a base isolation system consisting of 32 single-curvature friction pendulum bearings, manufactured by ALGA (see Ref. [1]). The fundamental nominal properties of the bearing involve a friction coefficient,  $\mu$ , of 5 %, an equivalent radius of curvature,  $R_{eq}$ , of 3500 mm and maximum displacement capacity,  $d_{max}$ , of 260 mm. A view of a standard isolation bearing is provided in Fig. 5, alongside the nominal design properties. Based on the nominal design parameters and on the mass of the system, the isolated system has an estimated secant fundamental period of approximately 3 s. A photograph of an installed FP device is provided in Fig. 6. Note that the FP bearings were protected by cover seals (removed in Fig. 6) composed of foam-like materials, which were wrapped circumferentially around each bearing and extended over the entire depth from the top of the supporting column to the underside of the isolated concrete slab.

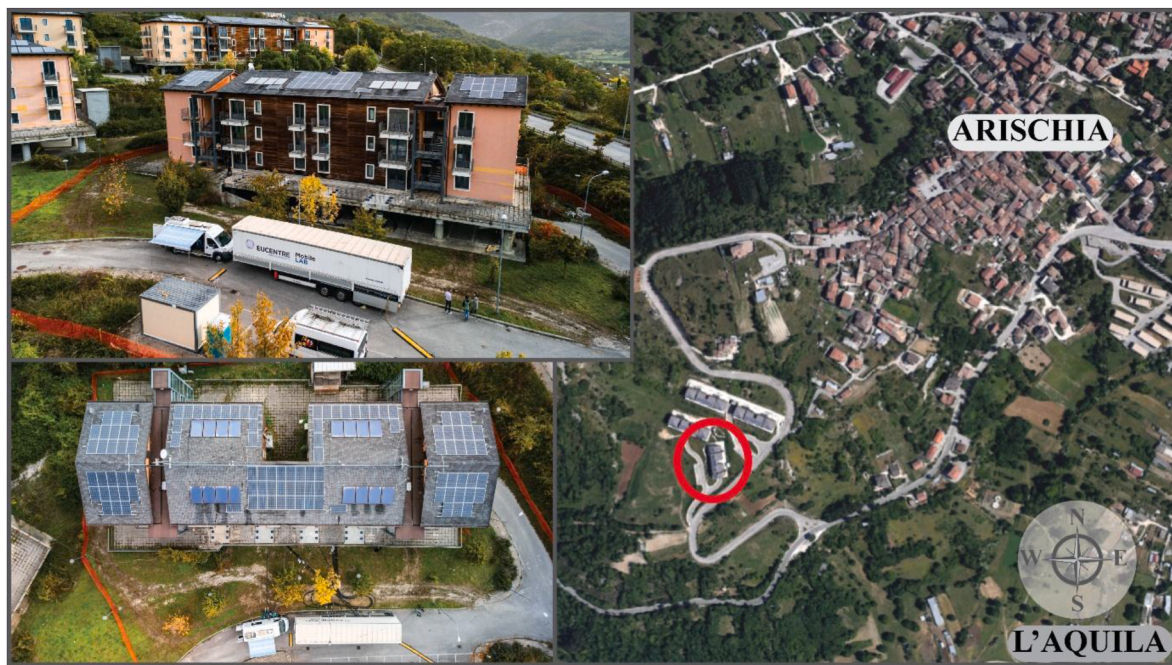


**Fig. 1.** Illustration and location of case study building.



**Fig. 2.** Photos of Case Study building.

### 3. Experimental setup

The case study building was loaded horizontally in the E-W direction by pushing/pulling the underside of the concrete slab supporting the superstructure, using four 1000 kN dynamic actuators. To achieve this, a

unique experimental setup was implemented on site that used the EUCENTRE's MOBILAB, in combination with a series of four self-reacting steel frames, intended to transfer the reaction forces generated by the actuators during the tests to the foundation (see Fig. 7).

The MOBILAB's main components are outlined in Figs. 8 and 9. The



**Fig. 3.** Case study technical drawings of first and second floor plan views.

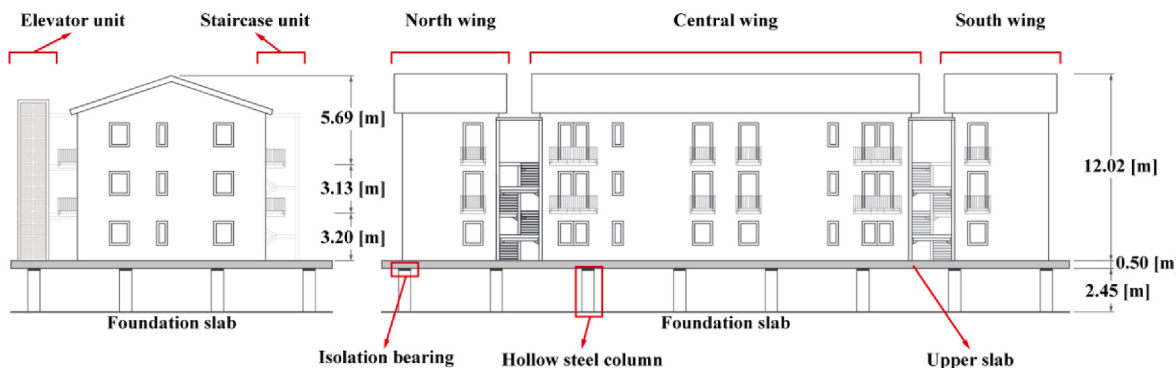


**Fig. 4.** Case study technical drawings lateral views.

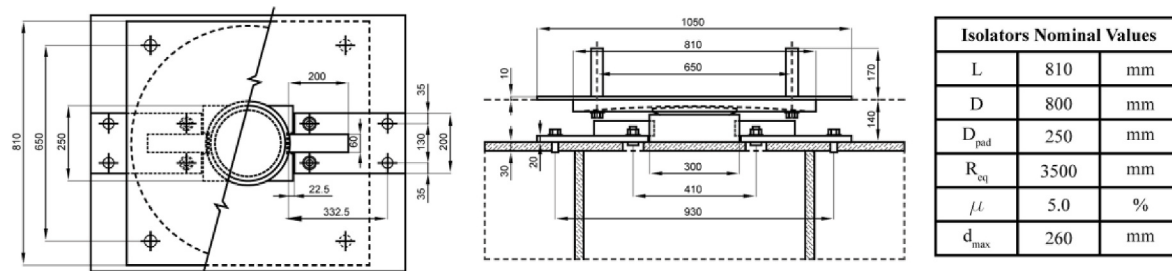


**Fig. 5.** Friction Pendulum Bearing Properties (all dimensions in [mm]).

system is equipped with:

- Four hydraulic actuators, each capable of delivering a dynamic force of 1000 kN and a displacement of  $\pm 250$  mm, in order to simulate dynamic displacements and accelerations (Fig. 8a);

- Hydraulic system, including pumps, reservoirs, accumulators, and piping, to ensure the required oil flow in the actuators (Fig. 8b and c);
- A control unit (Fig. 9), equipped with a digital controller, which supervises the system, generating and managing signals that coordinate the actuators during the testing phase, and with data acquisition stations;



**Fig. 6.** Isolation bearing placed on the top of the steel column.



**Fig. 7.** Actuator installed on reaction frame.

- A power unit, with a power of 800 KVA that ensures operational independence and efficiency.

The system can simulate dynamic scenarios, such as seismic events, with an oil flow capacity of approximately 6000 L/min. The achievable acceleration is 1.2 g for mobilized weights up to 150 tonnes, though this progressively decreases to 0.3–0.4 g for heavier systems. Transportability is ensured by three trailers housing the pumps, accumulators, power unit, and actuators, along with a van for the controller and data acquisition systems, enabling direct deployment to testing sites.

The steel reaction frames were designed to support the four actuators

and safely transfer their maximum force outputs whilst protecting the foundation structure from potential damage. In addition, the system was designed with modularity in mind to facilitate transportation and on-site assembly. The actuators were installed between the four central pairs of columns on the West side of the building.

The reaction frames were connected to the three columns aligned with the actuators, as illustrated in Fig. 10. As direct anchorage to the isolated slab was not feasible, a fastening system was devised, to transmit actuator forces while allowing slab movement. As a result, the reaction frame was split into two parts flanking the actuator: (i) an upper section, anchored to the isolated slab; and (ii) a lower section, anchored

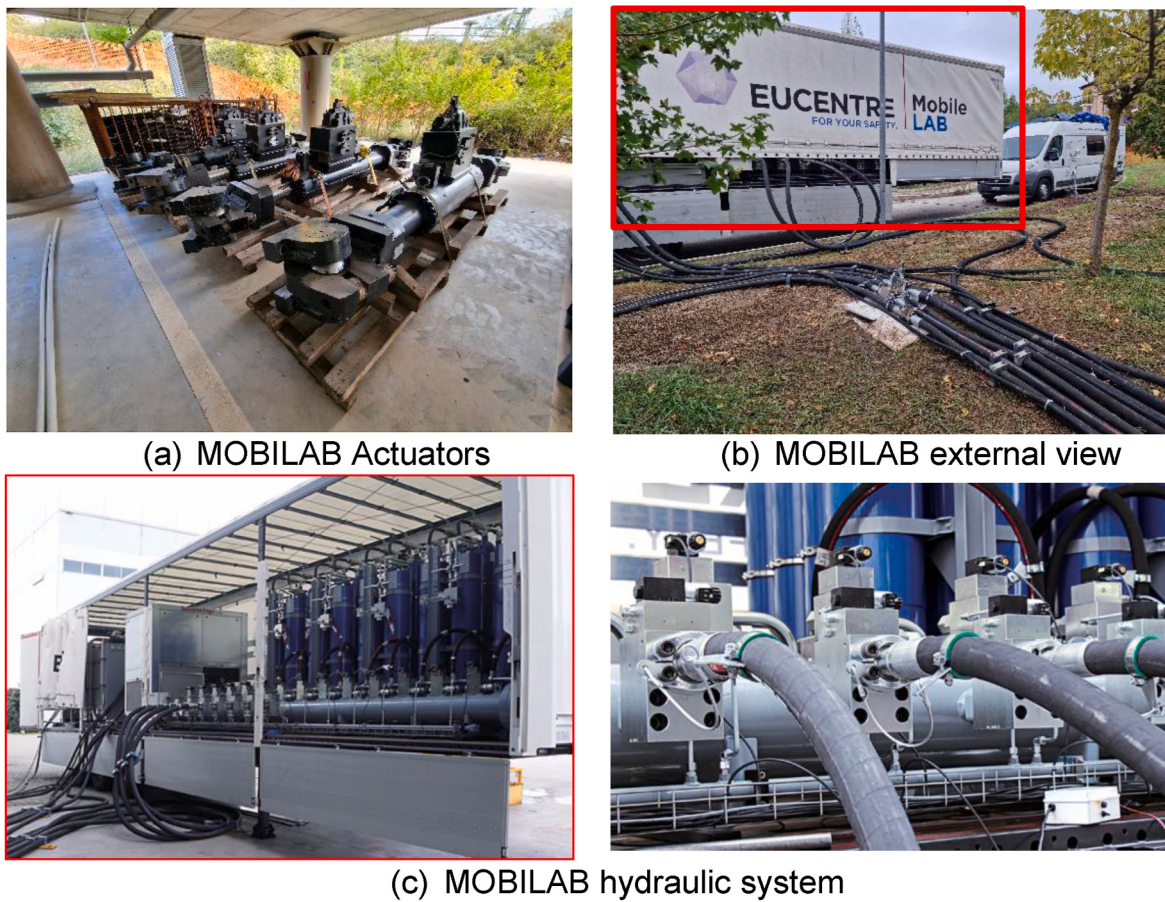


Fig. 8. View of MOBILAB main components.

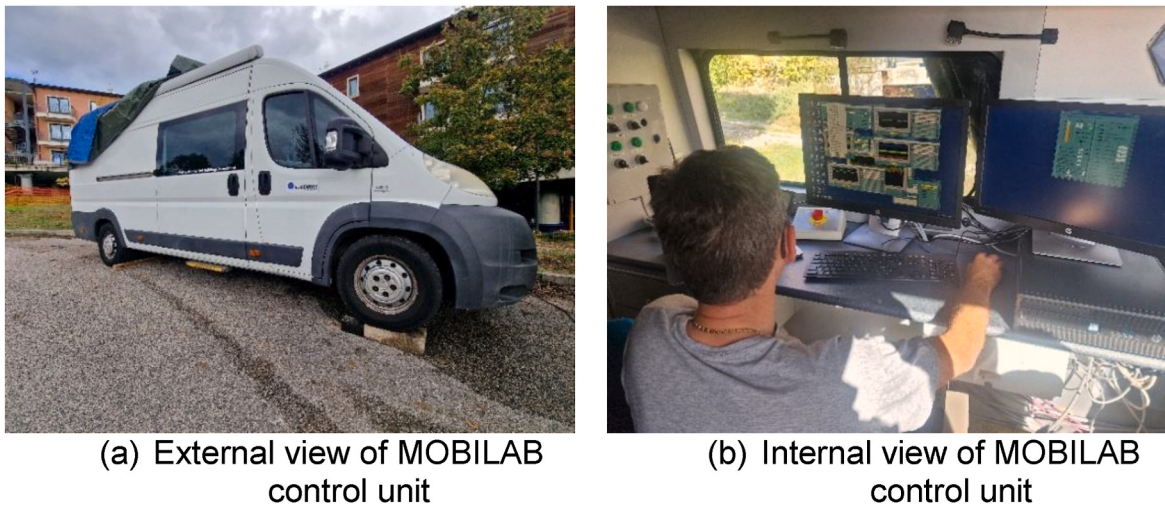


Fig. 9. Mobile control unit.

to the steel columns. The lower section incorporated a truss system to transfer forces to the column bases without causing damage. Retention rings were placed at the base of the outer columns and atop the central column. Paired steel profiles were used between these rings to ensure even stress distribution and prevent local instabilities. Fig. 10 illustrates the actuator's operating mechanism during push (blue) and pull (red) phases. The upper frame had a U-shape design to accommodate the relative displacement between the isolated slab and the columns. It consisted of two side elements aligned with the displacement direction

and a connecting beam for actuator mounting. Anchored with post-tensioned bars, the U-frame relied on friction connections to sustain applied forces, as depicted in Fig. 11.

To address fabrication and assembly tolerances, bolted connections were primarily used. The column-connected frame was subdivided for ease of transport. Each of the three rings was halved, enabling the use of spacers to accommodate imperfections. The rings were joined via a bolted truss made of HEB profiles and L-shaped bracing, designed to resist buckling. Given the unique requirements of this setup and the

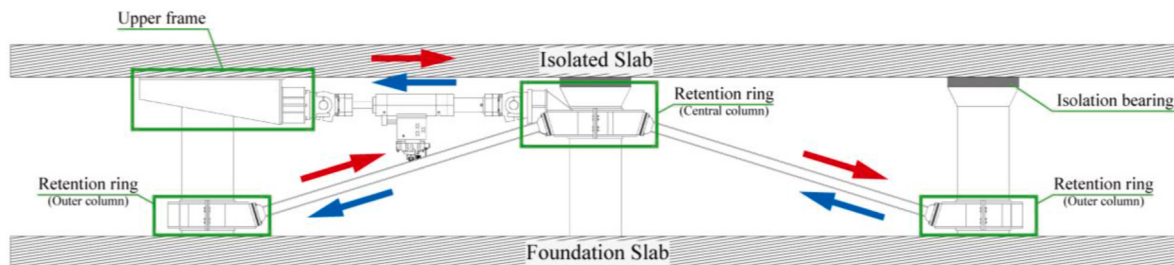


Fig. 10. Reaction frame force pattern.

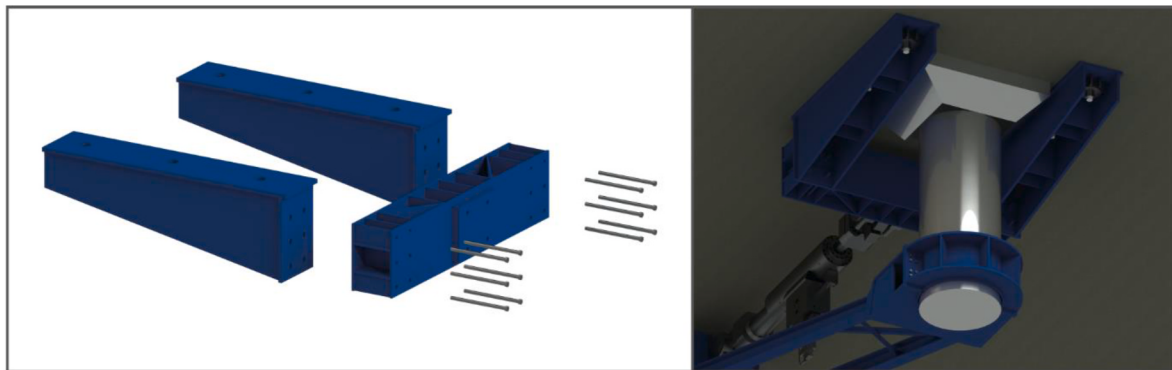


Fig. 11. Exploded view of the U-frame (left) and U-frame anchored to the bottom face of reinforced concrete slab (right).

MOBILAB's equipment, additional verifications of the design were carried out via detailed finite element analyses in Abaqus [40], in which the frame was modeled using brick elements. These simulations ensured that the designed setup could guarantee effective stress distribution, preventing overloading of the steel columns. Fig. 12 shows stress contours for the central ring. To ensure continuity and strength in the ring assemblies, full-penetration welds were used to connect the steel plates.

Fig. 13 shows a 3D rendering of the frame alongside its on-site implementation.

### 3.1. Instrumentation and data acquisition

The response of the case-study building was documented using a broad array of sensors, including load cells, three-axis accelerometers, and linear variable displacement transducers (LVDTs), installed at different locations on the reinforced concrete slab and the building, to monitor the structure's response continuously in time. High-resolution videos of select bearings across the isolation plan were also acquired to determine differential movement. Additionally, video recordings and

photographs were taken from various fixed points, as well as from Unmanned Aerial Vehicles (UAVs). Post-shake physical inspections were also performed before and after each test, with additional detailed high-resolution photographs.

A total of 49 channels were acquired, comprising 23 channels connected to the MOBILAB controller (all displacement transducers, 15 of which were dedicated to test setup control) and 26 channels connected to the external data acquisition system (including all accelerometers and two string potentiometers for superstructure inter-story drift monitoring). Most of the instrumentation was deployed at the slab level, arranged as shown in Fig. 14.

To monitor slab displacement relative to the ground in the E-W direction, four string potentiometers ( $\pm 1000$  mm stroke) were installed. Among these, LVDT 1 and LVDT 4 measured displacement at the NW and SW corners of the slab, respectively, while LVDT 2 and LVDT 3 were positioned on the East side, aligned with the actuator orientation. Specifically, LVDT 2 was placed midway between Actuators 1 and 2, and LVDT 3 between Actuators 3 and 4.

Additionally, two tracers (Tracer 1 and Tracer 2, in Fig. 14) were

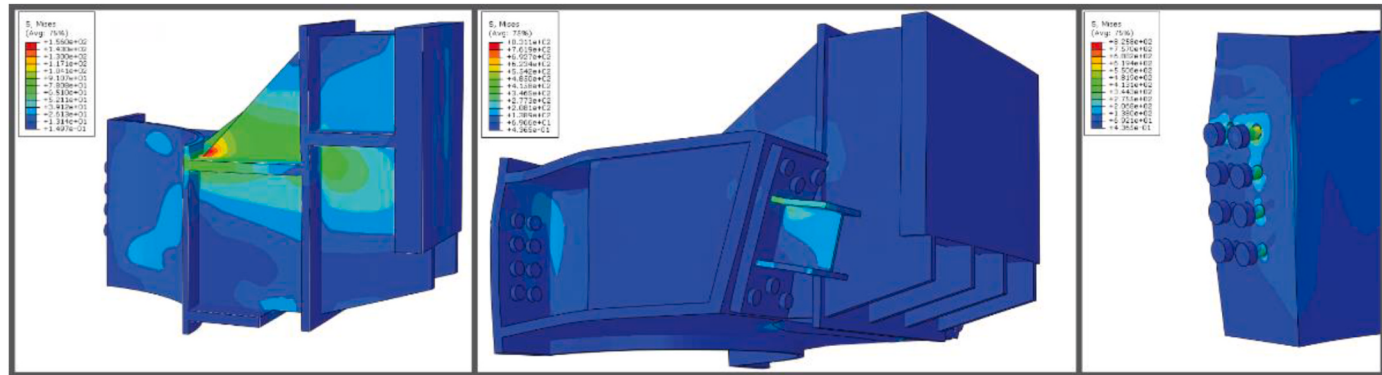


Fig. 12. FEM analysis carried out with Abaqus software to check the stress state of the components of the reaction frame and the steel columns at the base of the building.



Fig. 13. Comparison between 3D models and the constructed frame.

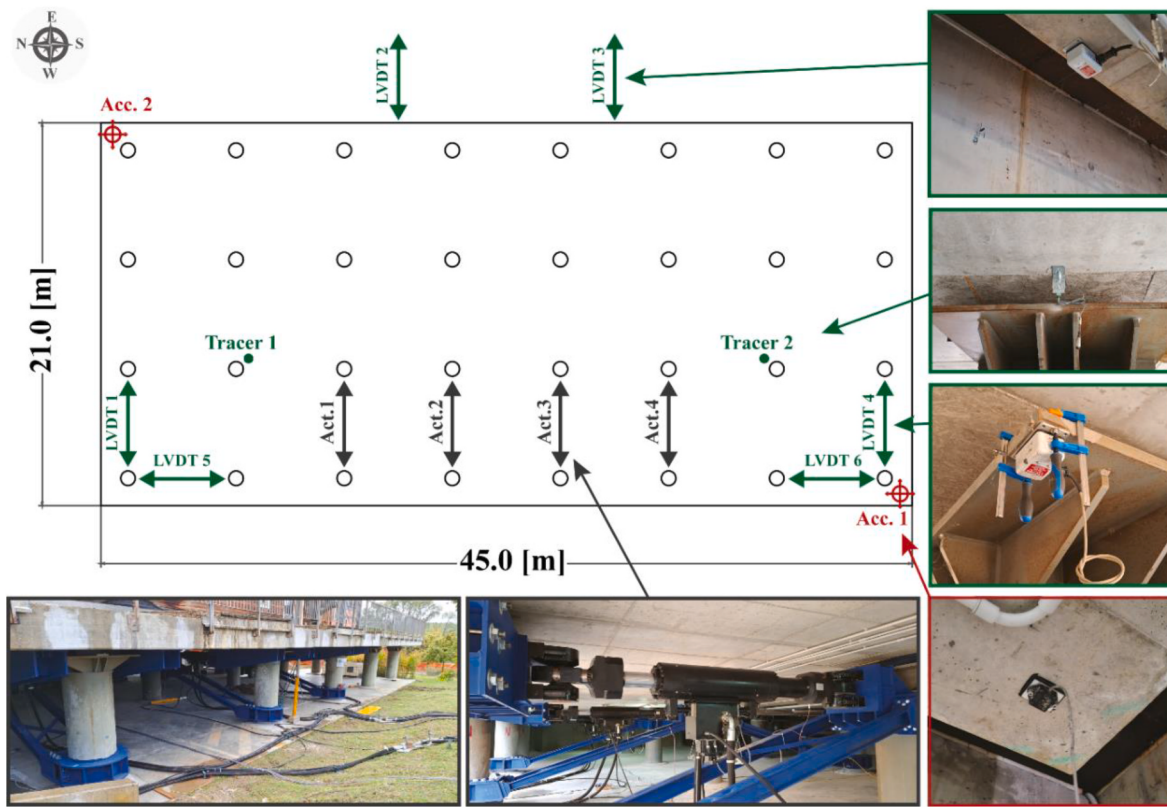


Fig. 14. Layout of the actuators and instrumentation at the isolated slab level.

used to monitor the relative displacement of the slab with respect to the top of the steel columns at two critical locations.

To capture displacement in the N-S direction, perpendicular to the actuator axis, two drag potentiometers ( $\pm 250$  mm stroke) were installed: LVDT 5 at the NW corner and LVDT 6 at the SW corner. Lastly, two dial gauges ( $\pm 25$  mm stroke) were installed to detect any vertical displacement of the slab. The displacements of the self-reacting steel

frames and the columns to which they were anchored were also monitored, to ensure they did not experience excessive deformations or movements due to the applied forces.

Two three-axis accelerometers were installed in the SW corner (Acc. 1) and NW corner (Acc. 2) of the slab. These accelerometers had an amplitude range of  $\pm 2$  g (at the slab, floor 1 and floor 2 levels) and  $\pm 6$  g (at roof level), frequency range of DC–200 Hz and a wide dynamic range

of 155 dB. Although the focus of the test was the behavior of the base isolation system, accelerometers were also installed at the center of each floor diaphragm.

### 3.2. Loading protocol

The loading protocol was selected with the main objective of assessing the response of the base isolation system. This was achieved by selecting a loading sequence consistent with EN15129 specifications [41], adopted in Europe to characterize the behavior of individual bearings via laboratory experiments. Hence, displacement-controlled, 3-cycle sinusoidal loading histories of varying amplitude and velocity were adopted. The testing amplitude varied from  $\pm 50$  mm to  $\pm 200$  mm corresponding to 25%–100% of the design displacement (i.e., 200 mm); the testing velocity varied from 50 mm/s up to a maximum velocity of 250 mm/s. This variety of sinusoidal cycles allowed for recording the system's response under various induced frequencies.

The results of the 12 tests summarized in the test matrix in Table 1 are discussed in this paper. Test IDs were assigned based on the peak loading amplitude (A) and the peak velocity (V) reached during each test. For instance, a field experiment performed considering a sinusoidal loading history characterized by maximum displacement amplitude of  $\pm 50$  and maximum velocity of 50 mm/s was designated A50V50. As shown in Table 1, some tests were repeated multiple times, namely tests A200V200 and A200V250 were each performed four times and two times, respectively, and distinguished with the suffixes A, B, C, etc.

## 4. Preliminary experimental results

This section presents preliminary results from the field testing, focusing on the response of the base isolation system and on the characterization of its performance. Due to the large volume of data acquired, selected representative tests are used to illustrate key experimental observations and outline the methodology adopted to derive the isolation system's properties from raw measurements. The experimental data alongside other pertinent information (e.g., drawings, lab reports) are available via the Built Environment Data Experiments platform [38].

The experimental characterization focused on evaluating the isolation system's static and dynamic friction coefficients, its stiffness before and after activation, and its energy dissipation and equivalent damping characteristics.

### 4.1. Force-displacement behavior of the isolation system

The central element in the system characterization is the force-displacement response of the base isolation system. This was extracted by processing the continuous readings from the actuators and motion sensors. The raw actuator force data, obtained from calibrated load cells,

include not only the resisting forces of the friction pendulum bearings but also the inertial component of the structure's dynamic motion. Therefore, to isolate the true bearing response, it was necessary to estimate and subtract the inertial force contribution.

Displacement data, obtained from Linear Variable Differential Transformers (LVDTs), were preferred over actuator stroke measurements as they more accurately captured the motion of the slab relative to the fixed reference system and were not impacted by any minor flexibility of the reaction frame system.

Fig. 16 shows the response of the four actuators for Test A200V200-A, with photographs of a selected bearing at key displaced configurations outlined in Fig. 17. The results showcase a consistent activation of the bearing system at forces between 500 and 600 kN per actuator (corresponding around 2200–2300 kN in total, or roughly 14–15% of the slab-building weight). Peak actuator forces reached approximately 800 kN, though not simultaneously, and the total system force at peak displacement (200 mm) was close to 2500 kN.

The force response displayed oscillatory behavior, which is commonly observed in such experimental setups and is likely associated with the control system's efforts to maintain synchronized actuator motion and to vertical forces fluctuation. Additionally, the system response was not entirely uniform in terms of generated forces. At the same imposed displacement, the northernmost actuator consistently recorded a force approximately 20%–25% higher than its southernmost companion. Furthermore, the post-elastic stiffness appeared to be slightly lower at the southern end. Although these observations are specific to Test A200V200-A, they reflect general trends observed across the full set of experiments.

### 4.2. Rotational displacement of the slab

In addition to translational movement, the isolated slab exhibited a small but measurable torsional response. Fig. 18 illustrates the measured displacements from LVDT1 and LVDT4 (see Fig. 15 for reference), as well as the derived rotational time history from run A100V100. The maximum rotation observed reached approximately 0.02°, a value consistent with other tests in the series (which were all in the range –0.1 to 0.08 deg). The origin of this rotational response likely lies in a combination of setup-related imperfections, minor differences in displacement of the actuators, and asymmetry in the superstructure.

It should be noted that friction pendulum systems are generally effective in limiting torsional motion, particularly in comparison to rubber isolators or fixed-base structures, some rotation may be expected and does not undermine the system's overall effectiveness. Given the relatively minor magnitude of the rotational response, the slab displacement used to define the global force-displacement behavior was computed as the average of the LVDT measurements along the main direction of applied loading.

### 4.3. Inertial force correction and acceleration filtering

To isolate the true force in the bearing system, the inertial component of the slab motion was removed from the total actuator force. The slab acceleration, required for this correction, was estimated from accelerometer readings placed at both ends of the slab. However, the raw acceleration data were contaminated with environmental noise and required careful processing before use.

Finite Impulse Response (FIR) bandpass filters [42,43] were designed and applied to the acceleration signals from each test. These filters were chosen for their linear phase characteristics, which avoid distortion of the signal's frequency content. Filter parameters were customized for each test to isolate the relevant excitation frequencies while effectively suppressing noise. Horizontal accelerations were filtered with the same parameters, while the vertical component required different tuning.

Fig. 19 shows the filtered acceleration time histories from Test

**Table 1**  
Loading protocol test matrix.

| Test ID    | Ampl.<br>[mm] | Max. Vel.<br>[mm/s] | Freq.<br>[Hz] | Protocol Reference            |
|------------|---------------|---------------------|---------------|-------------------------------|
| A50V50     | $\pm 50$      | 50                  | 0.159         | EN15129 (25 % of max displ.)  |
| A100V50    | $\pm 100$     | 50                  | 0.08          | EN15129 (50 % of max displ.)  |
| A200V50    | $\pm 200$     | 50                  | 0.04          | EN15129 (100 % of max displ.) |
| A100V100   | $\pm 100$     | 100                 | 0.159         | EN15129 (50 % of max displ.)  |
| A200V100   | $\pm 200$     | 100                 | 0.08          | EN15129 (100 % of max displ.) |
| A200V150   | $\pm 200$     | 150                 | 0.12          | EN15129 (100 % of max displ.) |
| A200V200-A | $\pm 200$     | 200                 | 0.159         | EN15129 (100 % of max displ.) |
| A200V200-B | $\pm 200$     | 200                 | 0.159         | EN15129 (100 % of max displ.) |
| A200V200-C | $\pm 200$     | 200                 | 0.159         | EN15129 (100 % of max displ.) |
| A200V200-D | $\pm 200$     | 200                 | 0.159         | EN15129 (100 % of max displ.) |
| A200V250-A | $\pm 200$     | 250                 | 0.199         | EN15129 (100 % of max displ.) |
| A200V250-B | $\pm 200$     | 250                 | 0.199         | EN15129 (100 % of max displ.) |

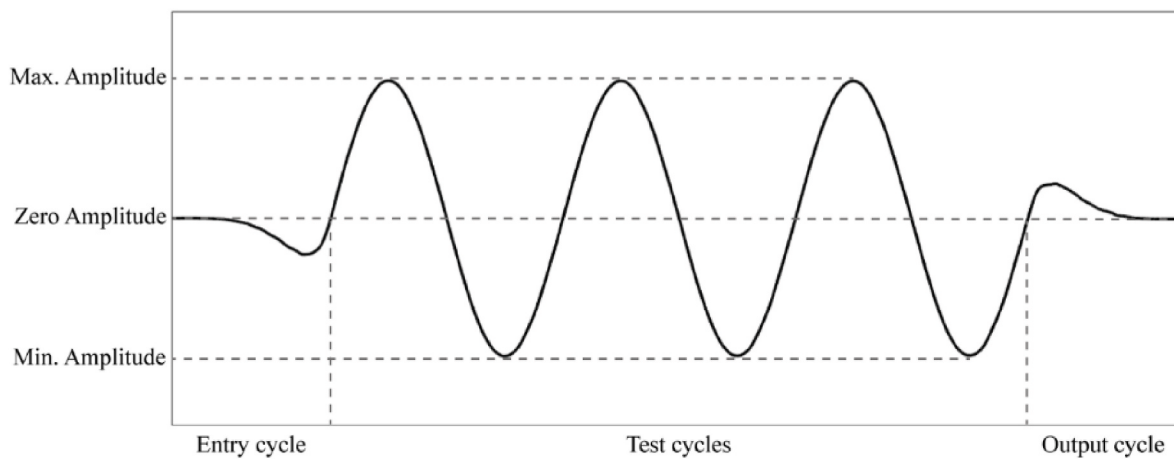


Fig. 15. Generic displacement sinusoidal cycle loading protocol.

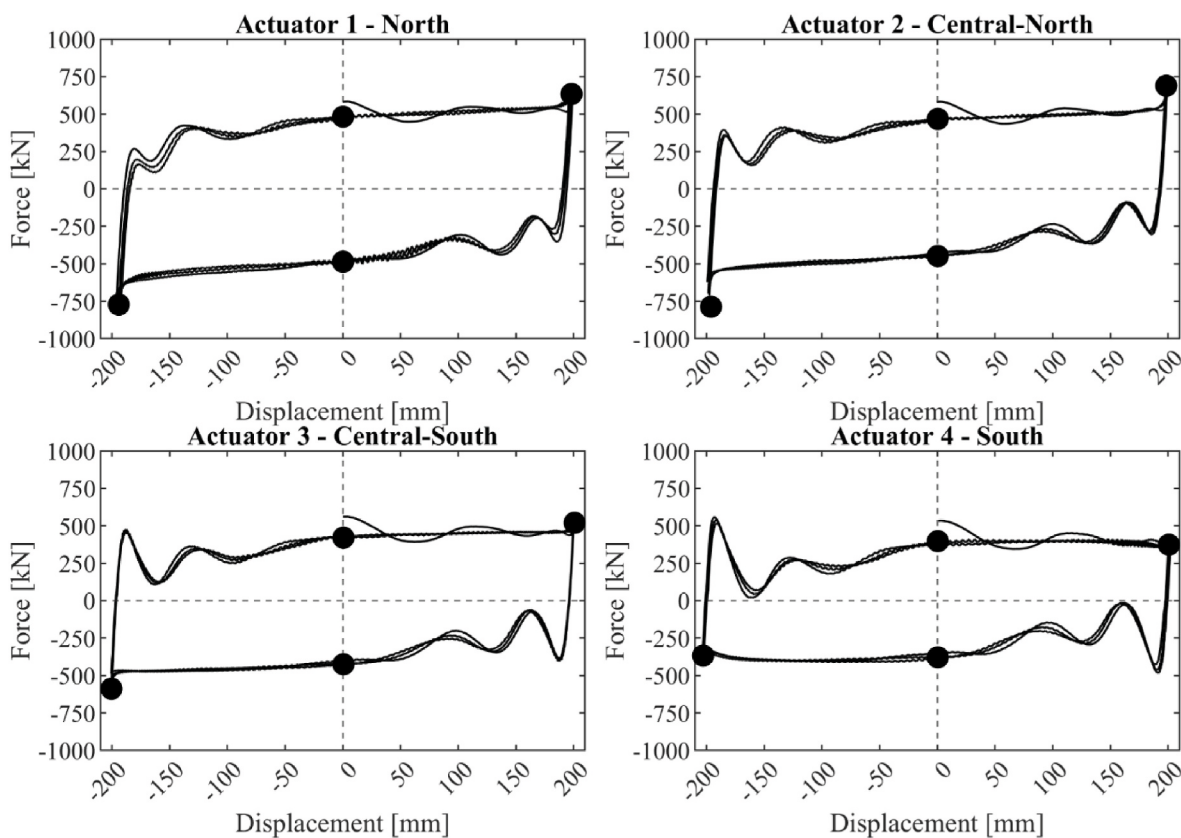


Fig. 16. Force-displacement plots for the actuators during Test A200V200-A.

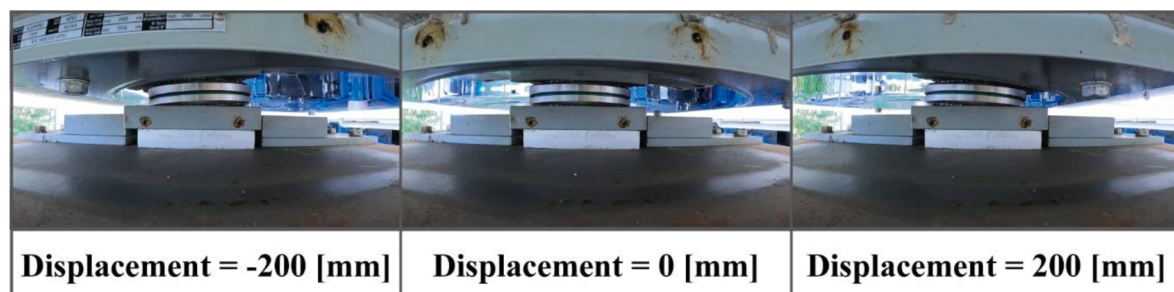
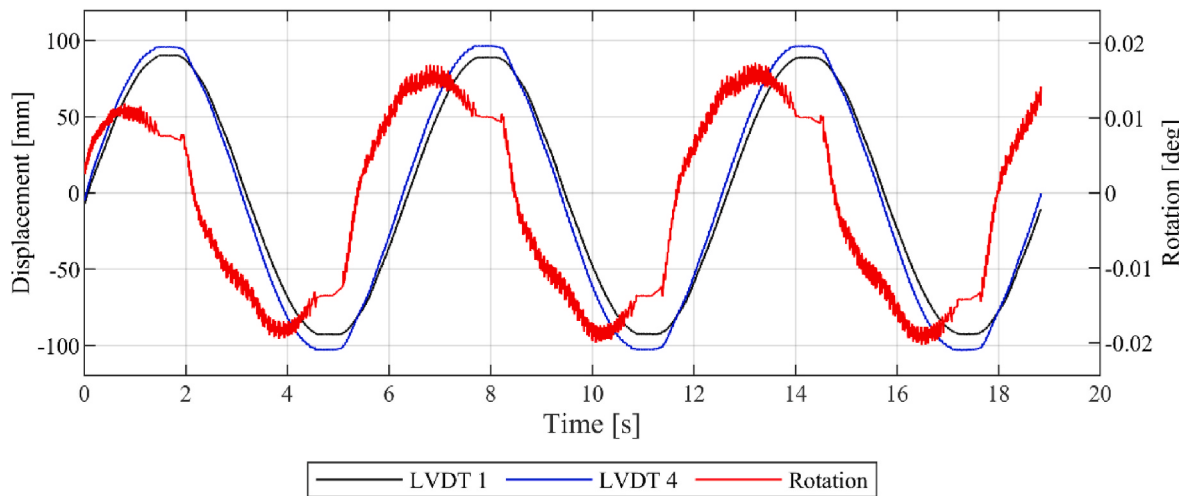
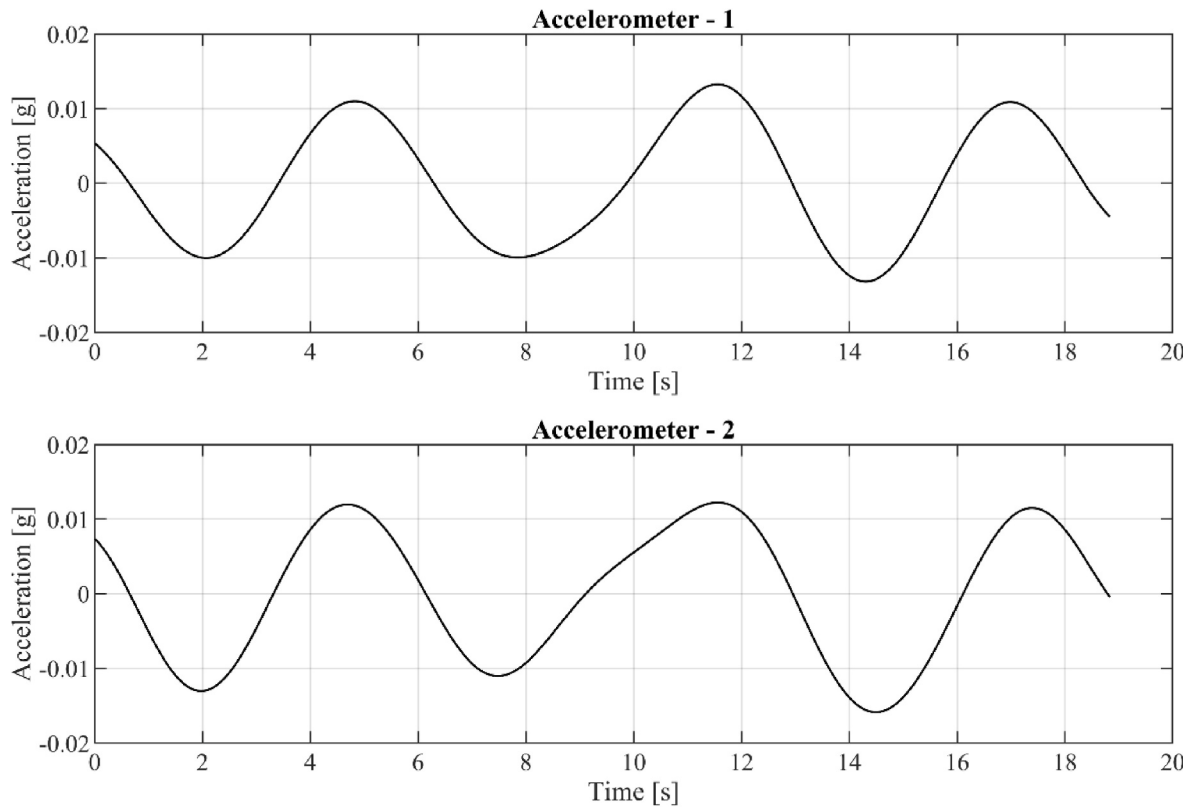


Fig. 17. View of one bearing at maximum negative displacement (left), maximum positive displacement (right) and zero displacement (center).



**Fig. 18.** Slab's rotation obtained from LVDT recordings during A100V100.



**Fig. 19.** Isolated slab filtered acceleration in the pushing direction during Test A100V100.

A100V100 at the slab level. The signals exhibit a clean sinusoidal shape, with peak amplitudes around 0.01g at both ends of the slab. Asymmetries between the signals, particularly higher negative peaks recorded by accelerometer 2, were considered plausible, given inherent structural irregularities and the complex test conditions.

The accuracy of the filtering process was verified by integrating the filtered acceleration signals using the trapezoidal method to obtain displacement time histories. These were compared with LVDT-based displacement measurements, as shown in Fig. 20. Good agreement was found, especially in the early cycles.

Once the acceleration was deemed accurate, the inertial force was calculated by multiplying the acceleration by the total mass of the structure. The net force acting on the bearing system was then obtained

by subtracting this inertial force from the total actuator force. These relationships are given as:

$$F_{IN} = a_{slab} \cdot M_{tot} \quad (1)$$

$$F_{FP} = F_{tot} - F_{IN} \quad (2)$$

Fig. 21 illustrates this correction, showing the total actuator force in black and the corrected bearing force in red. At peak displacement, the corrected force reached approximately 2000 kN, corresponding to about half the maximum capacity of the MOBILAB facility. Fig. 22 illustrates the corrected force-displacement response of the FPS for all the tests, grouped by test amplitude. The idealized curves shown were computed as discussed in the next section, based on the average post-elastic

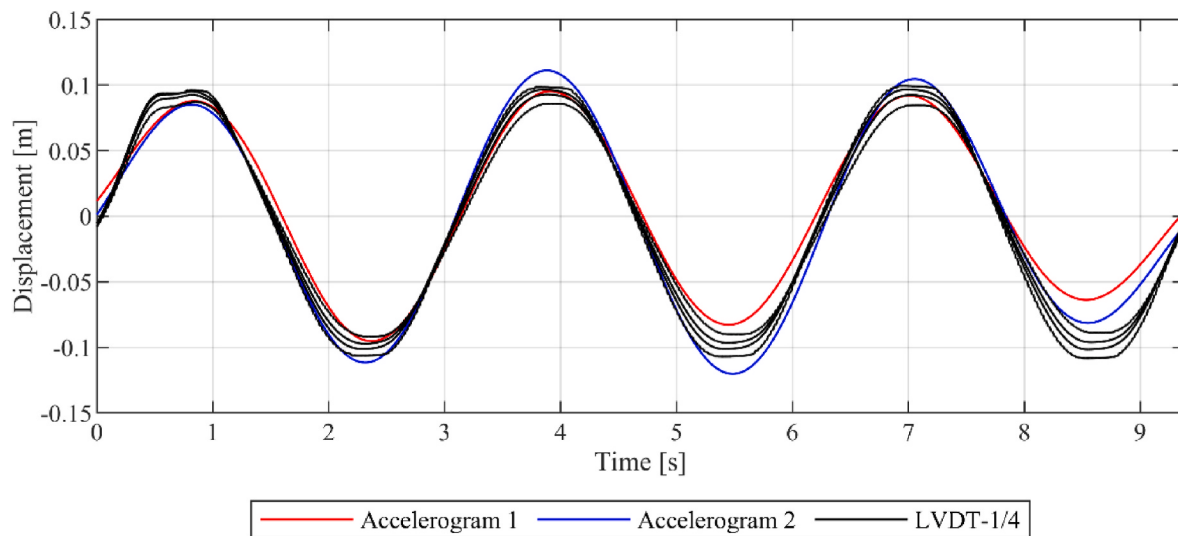


**Fig. 20.** Comparison of displacements retrieved from LVDTs and derived from acceleration records for Test A100V200.

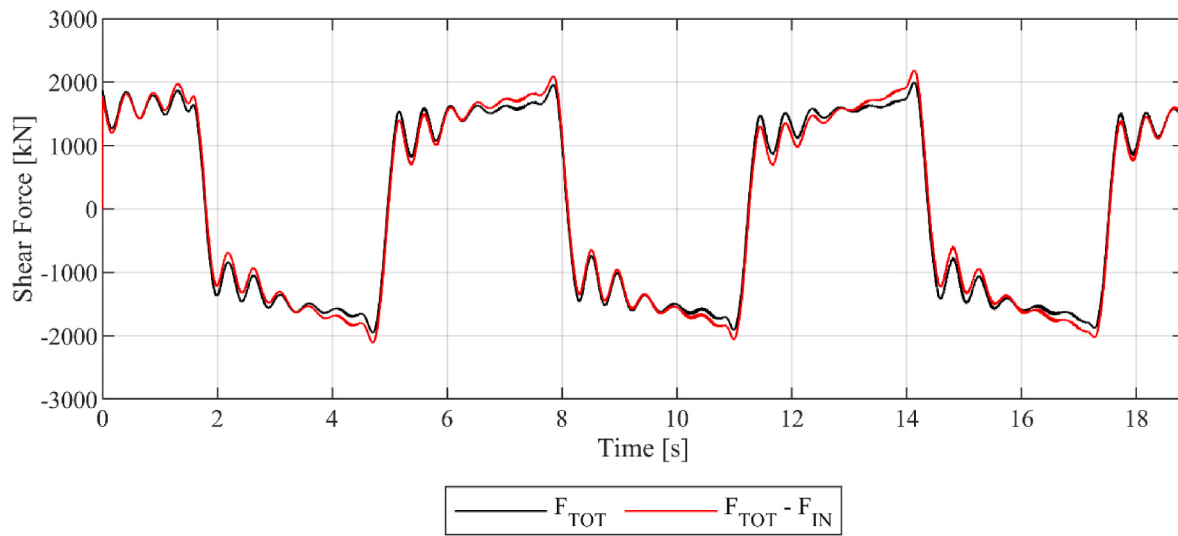


**Fig. 21.** Force-time plot during Test A100V100.

stiffness  $K_2$ , the friction coefficient from Eq. (4), and the weight of the isolated system (15,000 kN). A single set of these parameters was calculated for each group of tests characterized by the same displacement amplitude.

#### 4.4. Characterization of isolation system parameters

Following the extraction of the base isolation system's global response, a detailed characterization of its mechanical parameters was conducted. This included determining the post-elastic stiffness, friction coefficients, equivalent damping, and the effective seismic mass. The methodology adopted for this analysis is based on the framework proposed by Christopoulos and Filiatrault [44], with appropriate adaptations to the specific features of the current experimental setup.

To derive representative values from the numerous load cycles recorded in each test, a cycle-by-cycle analysis was performed. The entire force-displacement history was first segmented into individual cycles. Each of these was then processed to extract key mechanical parameters and to determine an average cyclic behavior representative of the test.

Fig. 23 illustrates the procedure used to obtain the average cycle

(black line) from the ensemble of individual cycles (gray lines) in Test A100V100. The idealized force-displacement curves were obtained in accordance with the procedure outlined in EN 15129. The post-elastic stiffness  $K_2$  was determined from the best-fit straight line obtained by least-squares interpolation of the experimental response between  $\pm 95\%$  of the negative and positive peak displacements ( $D_{\min}$  and  $D_{\max}$ ). Based on this stiffness, the reference point (Point 1) was identified by projecting the initial displacement onto the stiffness line. The subsequent characteristic points were then defined by combining the experimental force-displacement response with the  $K_2$  line: Point 2 corresponds to the peak on the positive side at  $D_{\max}$ , while Point 3 represents the intersection of the  $K_2$  line with the experimental curve on the positive branch. Similarly, Point 4 corresponds to the peak on the negative side at  $D_{\min}$ , while Point 5 is given by the intersection of the  $K_2$  line with the experimental curve on the negative branch. The area enclosed within the resulting idealized cycle was used to compute energy dissipation, friction, and equivalent damping in accordance with the equations reported below.

As an internal validation step, the seismic mass of the system was then back-calculated using the derived stiffness values, as shown in Equation (3). This mass calculation provided a consistency check against

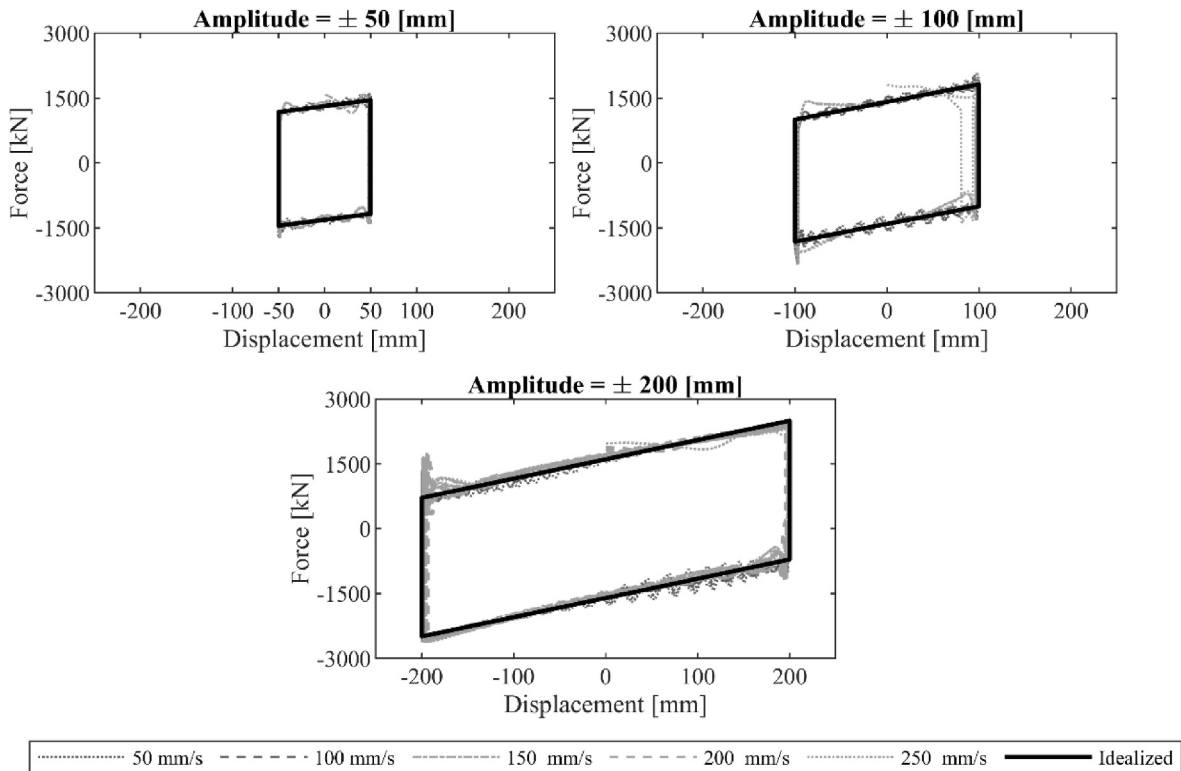


Fig. 22. Overall force-displacement response of base isolation system from all tests.

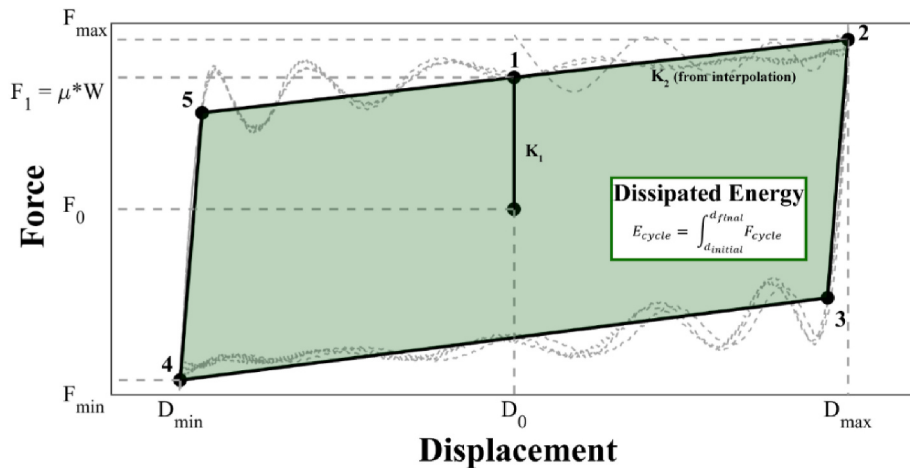


Fig. 23. Average cyclic behavior obtained from experimental data.

known physical properties of the slab-building system:

$$M = \frac{K_2 \cdot R_{eq}}{g} \quad (3)$$

Energy dissipation during each load cycle was computed as the area enclosed by the hysteresis loop. This was evaluated using numerical integration of the linearized actuator force over the displacement domain.

The dissipated energy was then used to derive two key parameters: the cycle-wise friction coefficient  $\mu_{cycle}$  and the equivalent viscous damping ratio  $\xi_{cycle}$ . These were computed using Equations (4) and (5), respectively:

$$\mu_{cycle} = \frac{E_{cycle}}{W \cdot 4 \cdot D_{max}} \quad (4)$$

$$\xi_{cycle} = \frac{E_{cycle}}{2 \cdot \pi \cdot D_{max} \cdot F_{max}} \quad (5)$$

where  $W$  is the total weight of the structure,  $D_{max}$  is the peak displacement in a given cycle, and  $F_{max}$  is the corresponding force.

Fig. 24 summarizes the evolution of friction coefficients computed via Eq. (4) across all cyclic tests, as a function of both testing amplitude and maximum testing velocity.

The friction coefficient increased with both testing amplitude and velocity, with a more pronounced upward trend observed as the testing velocity increased. Specifically, the coefficient increased from approximately 9.5 % at lower velocities (50 mm/s) to about 12 % at the upper end of the tested range. This behavior is consistent with previously reported findings [44], which indicate that friction coefficients tend to increase with increasing slip velocity until reaching a plateau. In the

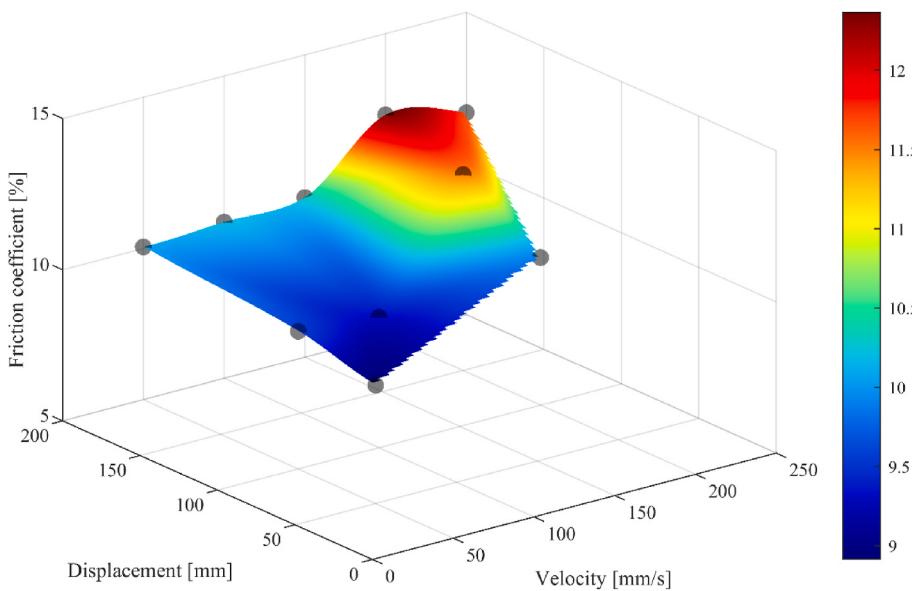


**Fig. 24.** Friction coefficient evolution during the test campaign.

present study, this plateauing trend appears to emerge in the 200–250 mm/s range, as shown in Fig. 24.

Fig. 25 shows the friction coefficient as a function of peak sliding velocity for the testing amplitude considered. Colored markers represent experimental data, with the solid black line indicating the mean trend, and the dashed line showing the theoretical model proposed by Fenz and Constantinou [45], outlined in Equation (6).

$$\mu(v) = \mu_{\max} - (\mu_{\max} - \mu_{\min}) \exp(-\alpha|v|) \quad (6)$$

Where  $\mu(v)$  is the coefficient of friction at velocity  $v$ ,  $\mu_{\max}$  and  $\mu_{\min}$  are the coefficients of friction at large velocity and nearly zero velocity, respectively, and  $\alpha$  is the rate parameter that controls the transition from  $\mu_{\min}$  and  $\mu_{\max}$ .

As seen above, the friction coefficient increases with velocity, particularly at higher amplitudes, with experimental variability reflecting amplitude-dependent effects. Equation (6) captures the overall trend, slightly overestimating friction at low velocities and underestimating it at high velocities, providing a reasonable first-order approximation of velocity-dependent friction.

The friction behavior of the system was further examined at specific points in each cycle. Pseudo-static friction coefficients were computed from the isolation system hysteretic response at points of zero velocity (i.e., peak positive and peak negative displacements), while dynamic friction coefficients were evaluated at maximum velocity, which typically occurs near zero displacement. Fig. 26 presents results from Test A200V250-A, showing the evolution of pseudo-static (blue), dynamic (red), and average cycle-based (dashed) friction coefficients. The pseudo-static friction values correspond to zero-velocity conditions, typically at peak displacements, while dynamic values were extracted at the points of highest velocity. Both pseudo-static and dynamic friction coefficients are approximately constant. The differences between the pseudo-static and dynamic values reflect velocity-dependent frictional effects. Importantly, the average friction coefficient derived from Equation (4) is consistently close to the dynamic values computed directly from the hysteretic response at points of zero displacement (i.e. maximum velocity).

Fig. 27 summarizes the evolution of equivalent damping ratios across all cyclic tests. Similar to the friction coefficient, the equivalent damping ratio exhibited an upward trend, increasing from approximately 36 %–45 % with rising velocity. This behavior aligns with the expected response of a Friction Pendulum (FP) system where, given a fixed radius of curvature and seismic weight (and thus a constant post-activation stiffness), the equivalent damping increases proportionally with the friction coefficient.

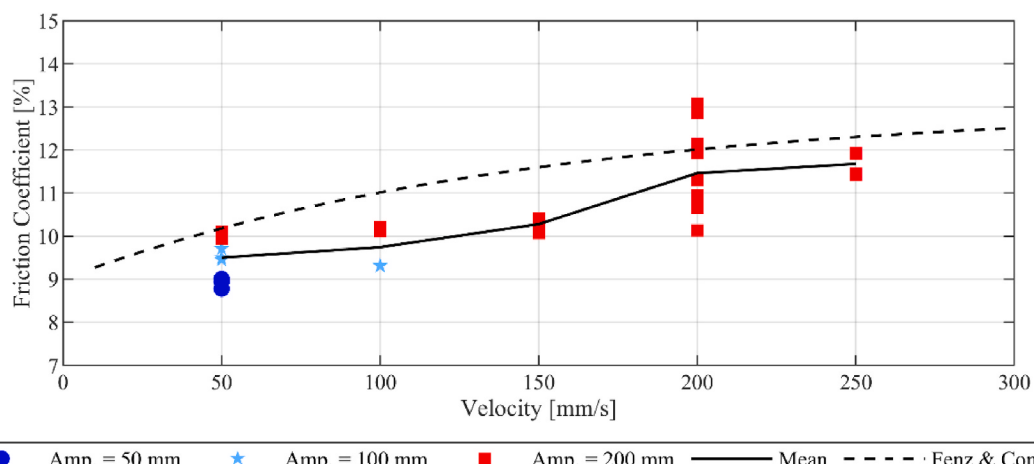


**Fig. 25.** Friction coefficient as a function of peak test velocity.

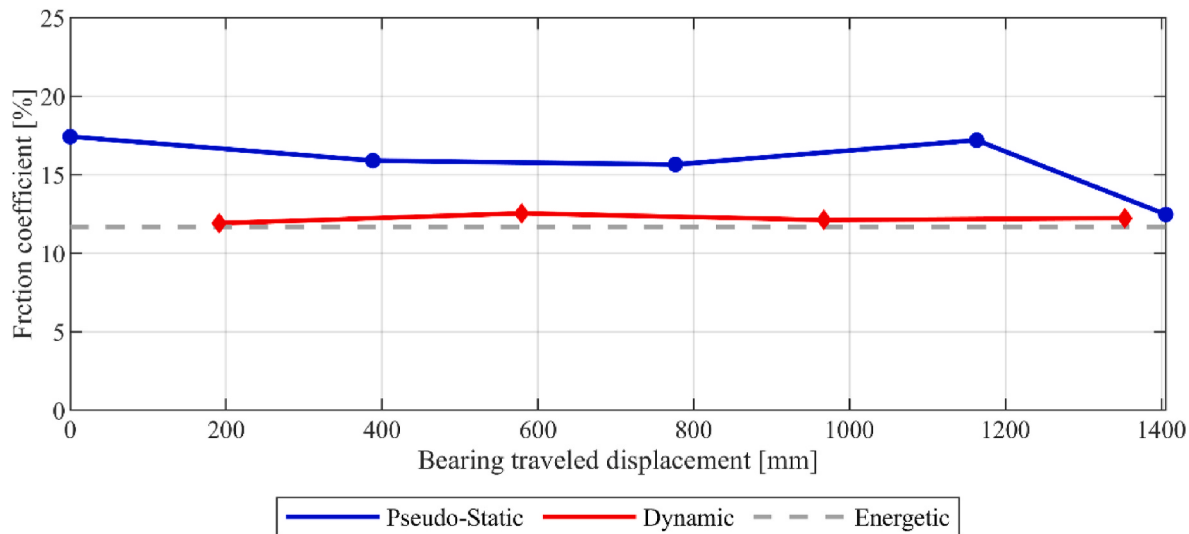


Fig. 26. Pseudo static and dynamic friction coefficient obtained during Test A200V250-A.

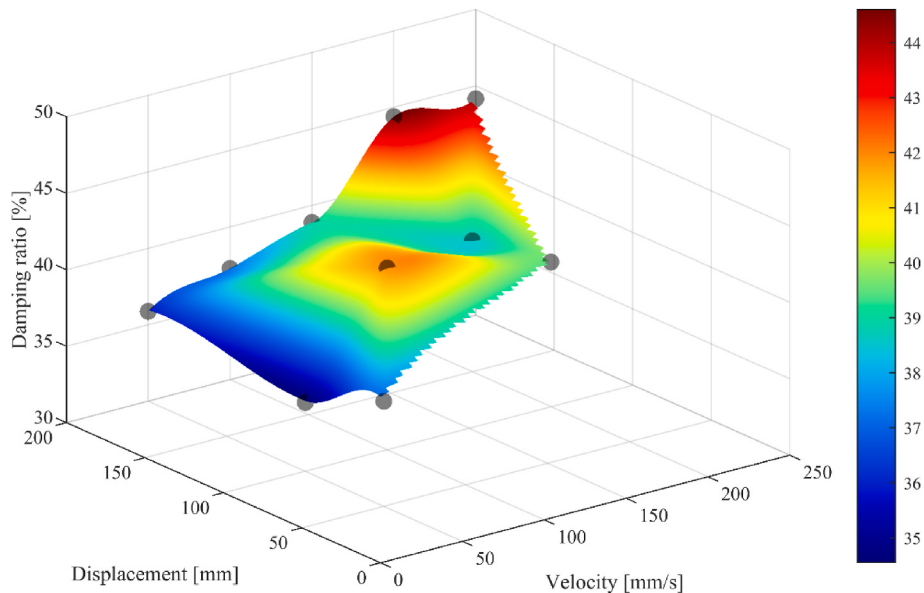


Fig. 27. Damping coefficient evolution during the test campaign.

Fig. 28 shows the post-elastic stiffness values obtained from the cyclic tests. The computed average stiffness was 4173 kN/m, with moderate dispersion that became somewhat more pronounced at higher testing frequencies. This outcome is consistent with expectations for friction pendulum bearings, where post-elastic stiffness is governed by the physical radius of curvature of the sliding surface and is calculated as the vertical load divided by that radius. Unlike parameters such as friction or material strength, this stiffness is a direct geometric property of the bearing and not expected to vary significantly. Based on the nominal bearing radius and structural weight, the theoretical post-elastic stiffness is approximately 4285 kN/m, less than 3 % higher than the test-derived average. While the discrepancy is minor in this case, small deviations from the theoretical value may stem from variations in axial load, unintentional tilting or rotation of the bearing end plates, or other sources of structural interaction. The reduction in stiffness observed at higher velocities may reflect rate-dependent behavior, such as inertial interaction effects, which warrant further investigation to confirm their influence and isolate their contribution.

The full set of tests yielded consistent trends in all principal

mechanical parameters. Table 2 compiles the key averaged results, including the average cycle-based friction coefficient, pseudo-static and dynamic friction values, post-elastic stiffness and equivalent damping. In all cases, the friction coefficients measured during testing were notably higher than the nominal value of 5 % provided by the manufacturer and assumed at the time of installation. This increase may be attributed to the natural aging of the isolators after more than 15 years of exposure to environmental conditions, which has likely altered surface characteristics and led to increased sliding resistance. However, literature reports (e.g., Ref. [1,46]) indicate initial experimental friction coefficients ranging from 5 % to 12 % for bearings from the same batch analyzed in this study. These values, measured approximately 15 years ago on brand-new isolators, are much more consistent with the values estimated in this study (approximately 9 %–13 %, according to Eq. (4)) and suggest that the increase in friction over time may be much less significant than that estimated based on comparisons with nominal friction coefficient values. While the observed increase in friction may also partly reflect natural wear accumulated over the course of the test program, repetitions of identical loading protocols (e.g., the A200V200

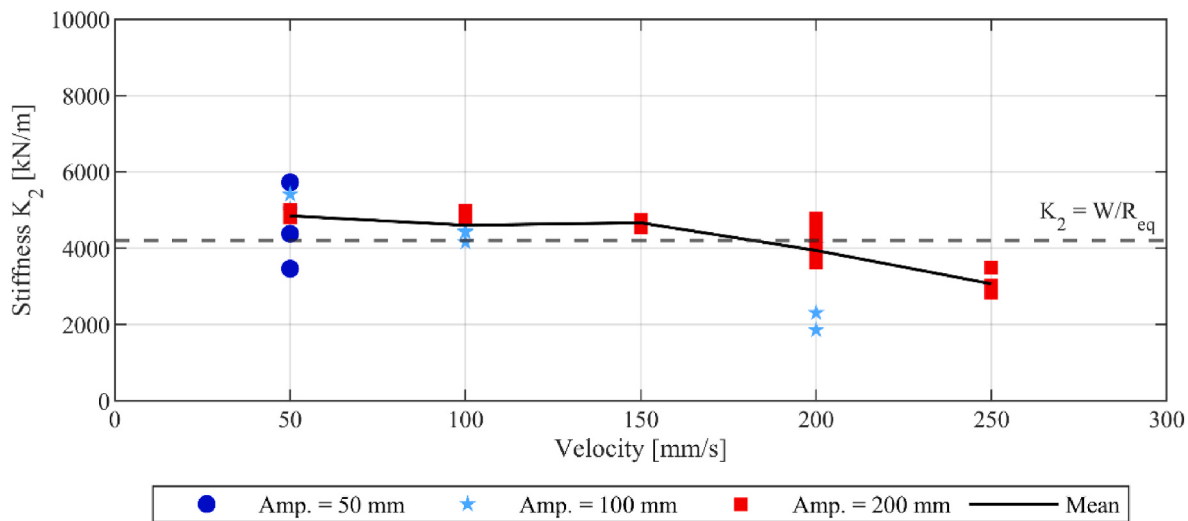


Fig. 28. Post elastic stiffness evolution during the test campaign.

**Table 2**  
Summary of data obtained from the field tests.

| Test       | $\mu_{cycle}$ [%] | $\mu_{static}$ [%] | $\mu_{dynamic}$ [%] | $K_2$ [kN/m] | $\xi_{eq}$ [%] |
|------------|-------------------|--------------------|---------------------|--------------|----------------|
| A50V50     | 8.89              | 15.12              | 10.76               | 4521         | 37.7           |
| A100V50    | 9.56              | 15.36              | 11.87               | 5134         | 34.95          |
| A200V50    | 10.05             | 16.69              | 10.48               | 4887         | 36.09          |
| A100V100   | 9.49              | 13.9               | 9.64                | 4342         | 45.76          |
| A200V100-A | 10.06             | 16.93              | 11.56               | 4865         | 37.75          |
| A200V150   | 10.26             | 16.58              | 11.76               | 4665         | 41.65          |
| A100V200   | 9.93              | 12.15              | 9.68                | 2750         | 38.07          |
| A200V200-A | 10.86             | 16.13              | 12.21               | 3967         | 45.58          |
| A200V200-B | 12.32             | 17.99              | 13.78               | 4355         | 46.34          |
| A200V200-C | 11.93             | 18.53              | 13.33               | 4595         | 44.47          |
| A200V200-D | 10.42             | 16.19              | 11.83               | 4042         | 44.81          |
| A200V250-A | 11.43             | 15.77              | 12.17               | 2878         | 45.63          |
| A200V250-B | 11.78             | 16.9               | 12.76               | 3254         | 44.97          |
| Avg.       | 10.53             | 16.01              | 11.67               | 4173         | 41.82          |
| St. Dev.   | 1.05              | 1.66               | 1.26                | 770          | 4.26           |
| COV (%)    | 9.97              | 10.40              | 10.87               | 18.45        | 10.19          |

series) did not show any consistent increase in measured friction, indicating that any friction increase induced by the experiments was minimal. More in-depth analysis is needed before definitive conclusions can be drawn. The complete dataset, representing a rare and extensive experimental effort, is made available to support future in-depth analysis by the research community.

The computed equivalent damping ratios were also higher than values normally attributed to FP bearings (typically lower than 30 %). However, the estimated equivalent damping coefficients are consistent with the measured friction values, which exceed the nominal friction coefficient by 2–3 times. Note that, with  $\alpha$  being the ratio between the force in the base isolator at maximum displacement and the force at motion inception, another way to estimate the equivalent damping ratio from the idealized hysteretic response of the bearing is:

$$\xi_{e,FP} = \frac{2}{\pi\alpha} \quad (7)$$

Equation (7) clearly shows that the equivalent damping coefficient is greatly influenced by the parameter  $\alpha$ , which is strongly correlated to the friction coefficient at play. For a given post-activation stiffness ( $W/R$ ), higher friction means lower  $\alpha$  and vice versa. The lower the value of  $\alpha$ , the higher the resulting equivalent damping. For example, for  $\alpha = 1$  the equivalent damping ratio is as high as 64 %, while for  $\alpha = 3$ , the damping ratio drops to 21 %. The tests conducted were characterized by  $\alpha$  values ranging from 1.2 to 1.8, which correspond to theoretical

damping coefficients in the range 35 %–53 %, well in line with the values reported in Table 2.

#### 4.5. Base isolation system: measured vs design properties

The research team encountered difficulties in retrieving precise information regarding the original properties of the Friction Pendulum (FP) bearings installed in 2009. As previously noted, substantial uncertainty surrounds the friction coefficients characterizing these devices at the time of installation. Available documentation reports values ranging from 5 % to 12 % but does not specify the exact coefficients for the bearings used in this project. Consequently, this limits the ability to draw definitive conclusions at this stage, regarding time-dependent property changes and their impact on long-term performance.

Nonetheless, the measured response of the isolation system can be contextualized by comparing it to the nominal properties of the FP bearings assumed during the original design phase. According to the literature (e.g., Ref. [1,47]), the preliminary design was conducted based on the NTC 2008 [48] displacement spectrum corresponding to a 1000-year return period, conservatively scaled for soil type E (i.e., soft soil conditions prone to seismic amplification). This spectrum exhibits a corner period of 3.0 s and a corresponding displacement of 0.41 m.

The base isolation system was developed using **Direct Displacement-Based Design (DDBD)** principles, following the framework proposed by Priestley et al. [49]. The resulting configuration included the 32 FP bearings, whose design properties are summarized Fig. 5 and in Table 3, for the whole system of bearings. While some sources (e.g., Ref. [1]) suggest that a friction coefficient of 3 % was considered in design, a value of 5 % is adopted here for consistency and to facilitate direct comparison. Table 3 contrasts the original design parameters with the “as-measured” average values from the 2024 field testing (i.e., this study). Note: friction coefficient and post-activation stiffness values are extracted from Table 2).

To assess system response using both sets of parameters, a displacement-based assessment procedure is applied, following the iterative method of Priestley et al. [49]. The analysis begins with an

**Table 3**  
FP system design and (average) measured properties.

| Property       | Design (2009) | Measured (2024) |
|----------------|---------------|-----------------|
| $\mu$          | 5 %           | 10.5 %          |
| $K_2$ [kN/m]   | 4285          | 4173            |
| $W$ [kN]       | 15000         | 15000           |
| $F_{act}$ [kN] | 750           | 1579.5          |

assumed peak displacement induced by the design-level seismic event. From the known friction coefficient, post-elastic stiffness, and seismic mass, the corresponding horizontal force and secant stiffness are computed. These yield the system's effective period and hysteretic behavior, from which the equivalent damping and corresponding spectral reduction factor are derived.

The 5 %-damped elastic response spectrum is then modified to reflect the effective damping, and the updated displacement demand is extracted based on the calculated effective period. If the resulting demand does not match the assumed displacement, the procedure is repeated until convergence is achieved.

Using the **design properties**, the estimated displacement demand under the 1000-year event is 207 mm. This results in an activation force of 750 kN and a peak horizontal force of 1641 kN, which is about 11 % of the structure's weight. The equivalent viscous damping is approximately 29 %, leading to a Eurocode [50] spectral reduction factor of 0.55, computed using:

$$\eta = \sqrt{\frac{10}{5 + \xi}} \geq 0.55 \quad (7)$$

Assuming a rigid superstructure, the effective period is approximately **2.76 s**.

In contrast, applying the **as-measured properties**, the displacement demand under the same seismic input is reduced to 153 mm, about 74 % of the original design displacement. The response yields an activation force of 1579.5 kN and a peak force of 2221 kN, or about 15 % of the structural weight. This represents a 35 % increase in force demand compared to the nominal design case.

The measured parameters also result in **effective damping of 46 %**, approximately 1.55 times the design value. However, the corresponding spectral reduction factor remains at **0.55**, due to Eurocode limits. The effective period is reduced to **2.04 s**, primarily due to the elevated friction coefficient. Fig. 29 compares the seismic demands and hysteretic responses for the design-based and measured systems. The comparison highlights important implications regarding the sensitivity of base-isolated structures to in-service properties.

While the **post-activation stiffness** closely matches theoretical predictions based on the radius of curvature and seismic weight, the **friction coefficient** is significantly higher than the manufacturer's nominal value assumed in design. Although it is currently unclear whether this increase is attributable to aging, surface contamination, or other in-service effects, its impact is notable. Higher friction delays isolator activation and increases force transmission to the superstructure, while also reducing self-centering capacity. At the same time, the increased damping, and the higher resistance result in lower displacement demand for a given seismic event.

It is noteworthy that, despite these discrepancies, the **base isolation system performed remarkably well**. The isolators provided substantial energy dissipation capacity and retained adequate displacement capacity with significant margin. Even with the elevated friction, the isolation system would effectively protect the structure against strong seismic events. This outcome is particularly notable given that it was **demonstrated through full-scale, in-situ testing on a real building**, offering direct evidence of long-term base isolation performance in real-world conditions.

These findings underscore the **critical importance of periodic performance assessments and accurate property characterization** of isolation systems over their service life, indicating that ensuring up-to-date knowledge of isolator behavior is essential for reliable seismic performance and informed decision-making in long-term building safety and resilience planning.

## 5. Summary and conclusions

This paper has presented the preliminary findings of the PASFIT project, a landmark international research initiative focused on the performance of base-isolated buildings under multi-cycle sine wave loadings at prescribed displacement amplitudes. Through an extensive in-situ testing campaign of a three-story residential structure in Arischia (L'Aquila, Italy), isolated with Friction Pendulum bearings and in continuous operation for over 15 years, this study has generated rare and valuable field data that address a critical gap in current seismic isolation research.

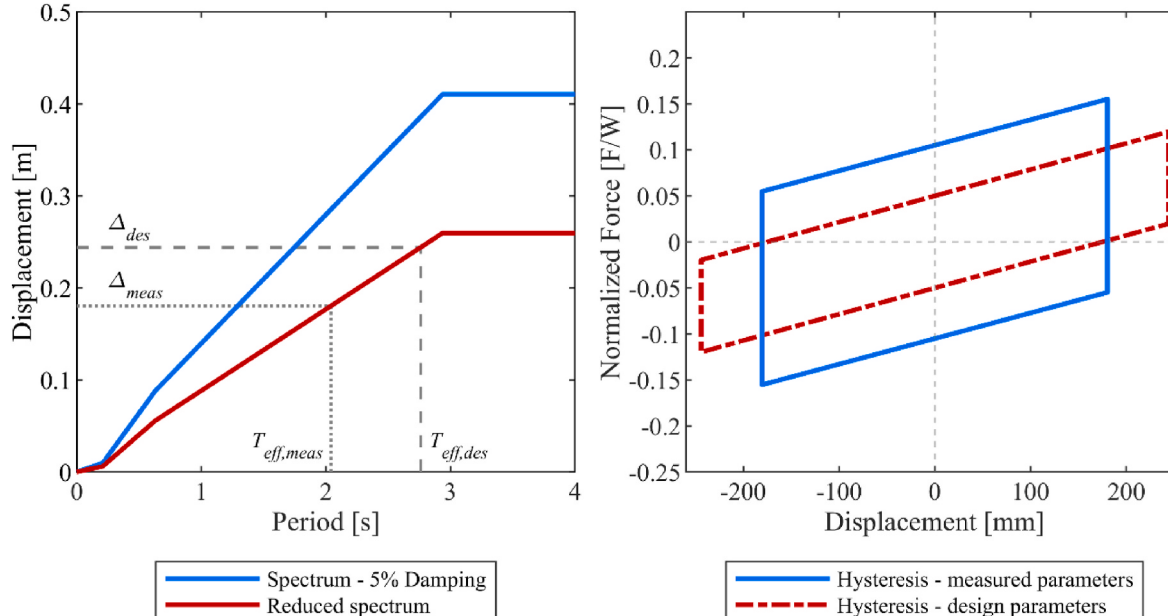


**Fig. 29.** Design seismic input at the site (left) and assessed FP system normalized force-displacement response (right).

Using a test setup involving custom self-reacting frames and the EUCENTRE's mobile laboratory, over 20 displacement-controlled loading protocols were applied to extract key mechanical parameters of the base isolation system. These include friction coefficients (both static and dynamic), post-elastic stiffness, energy dissipation, and equivalent damping, all derived from cycle-by-cycle analyses of force-displacement and acceleration data. A consistent trend of increased frictional resistance relative to nominal design values was observed, along with post-elastic stiffness values that aligned closely with theoretical expectations.

These results provide one of the few field-based experimental datasets capturing the aging behavior of FPS isolators at the system level. While the findings offer early insight into the effects of prolonged service on frictional and stiffness properties, they remain preliminary. Although a comprehensive evaluation falls beyond the scope of this paper, which is primarily focused on documenting key elements of the experimental program and on presenting preliminary observations drawn from field data, additional analyses, including comparisons with component-level tests, environmental condition records, and advanced modeling, are needed and will be performed in the future to fully understand the implications for seismic performance and design assumptions.

It should be noted that, because the imposed displacement histories replaced inertial forces with actuator reaction forces, the tests conducted in this program did not capture the full interaction between mass, damping, and stiffness that occurs under earthquake excitation. While the applied protocols included a range of velocities to assess velocity-dependent friction effects, the absence of dynamic coupling with the superstructure may lead to a slight (up to approximately 10 %) overestimation in the measured friction coefficient, and a 5–10 % underestimation or alteration in the apparent equivalent stiffness compared to values under true seismic loading [51]. The results should therefore be interpreted as characterizing the isolation system under controlled, displacement-driven conditions, similar to standard bearing tests conducted in the laboratory, rather than as direct predictions of the full structural response.

It should also be noted that the findings presented in this study are based on a single three-story building equipped with a single type of friction pendulum isolation system, tested under constant vertical load conditions. While the results provide valuable field-based insight into the behavior and aging of this system, they should be interpreted with caution when extending to different isolation types, building configurations, or service conditions.

Overall, the PASFIT project demonstrates the feasibility and value of conducting rigorous in-situ testing on aged isolation systems. The data generated serve as a crucial resource for improving the reliability of performance-based assessments and updating seismic design practices to account for long-term effects. Future work will continue to expand upon these findings, with the goal of delivering more definitive conclusions and practical recommendations for the engineering community.

#### CRediT authorship contribution statement

**P.M. Calvi:** Writing – review & editing, Writing – original draft, Supervision, Project administration, Methodology, Funding acquisition, Conceptualization. **A. Rapone:** Writing – original draft, Investigation, Formal analysis, Data curation. **T.C. Becker:** Writing – review & editing, Funding acquisition, Conceptualization. **H. Sucuoglu:** Writing – review & editing, Funding acquisition. **G. Gabbianelli:** Writing – original draft, Supervision. **B. Chalarca:** Writing – original draft, Supervision. **I. Lanese:** Writing – review & editing, Software, Resources. **G.J. O'Reilly:** Writing – review & editing, Project administration. **E. Rizzo-Parisi:** Software, Resources. **F. Dacarro:** Supervision, Software, Resources.

#### Declaration of competing interest

The authors declare that they have no known competing financial

interests or personal relationships that could have appeared to influence the work reported in this paper.

#### Acknowledgements

This work is part of the transnational access project "ERIES-PASFIT", supported by the Engineering Research Infrastructures for European Synergies (ERIES) project ([www.ries.eu](http://www.ries.eu)), which has received funding from the European Union's Horizon Europe Framework Programme under Grant Agreement No. 101058684.

This is ERIES publication number J8. The contributions of the technical staff at Eucentre are sincerely appreciated for their dedication and expertise throughout the experimental campaign. The authors also wish to express their gratitude to the Italian Civil Protection Department and the local authorities of the L'Aquila province for their invaluable cooperation and logistical support.

#### Data availability

Data will be made available on request.

#### References

- [1] Calvi GM, Spaziante V. Reconstruction between temporary and definitive: the CASE project. *Progettazione Sismica* 2009;3:221–50.
- [2] Kaatsiz K, Alıcı FS, Sucuoğlu H, Tanışer S, Kale Ö. Seismic performance assessment of base isolation systems in five hospitals during the Mw7.8 and Mw7.6 2023 earthquakes in Southeast Turkey. *Earthq Spectra* 2024;41(1):176–97. <https://doi.org/10.1177/87552930241284613>. 2024.
- [3] Fenz DM, Constantinou MC. Behaviour of the double concave friction pendulum bearing. *Earthq Eng Struct Dynam* 2006;35:1403–24.
- [4] Fenz DM, Constantinou MC. Spherical sliding isolation bearings with adaptive behavior: experimental verification. *Earthq Eng Struct Dynam* 2008;37(2):185–205.
- [5] Morgan TA, Mahin SA. Achieving reliable seismic performance enhancement using multi-stage friction pendulum isolators. *Earthq Eng Struct Dynam* 2010;39(13):1443–61.
- [6] Tsai CS, Lin YC, Su HC. Characterization and modeling of multiple friction pendulum isolation system with numerous sliding interfaces. *Earthq Eng Struct Dynam* 2010;39:1463–91.
- [7] Kumar M, Whittaker AS, Constantinou MC. Characterizing friction in sliding isolation bearings. *Earthq Eng Struct Dynam* 2015;44:1409–25.
- [8] Becker TC, Bao Y, Mahin SA. Extreme behavior in a triple friction pendulum isolated frame. *Earthq Eng Struct Dynam* 2017. <https://doi.org/10.1002/eqe.2924>.
- [9] Bao Y, Becker TC, Hamaguchi H. Failure of double friction pendulum bearings under pulse-type motions. *Earthq Eng Struct Dynam* 2017;46:715–32.
- [10] Fenz DM, Constantinou MC. Spherical sliding isolation bearings with adaptive behavior: theory. *Earthq Eng Struct Dynam* 2008;37(2):163–83.
- [11] Becker TC, Mahin SA. Experimental and analytical study of the bidirectional behavior of the triple friction pendulum isolator. *Earthq Eng Struct Dynam* 2012;41(3):355–73.
- [12] Timinsina S, Calvi PM. Variable friction base isolation systems: seismic performance and preliminary design. *J Earthq Eng* 2018;25(1):93–116. <https://doi.org/10.1080/13632469.2018.1504837>.
- [13] Yang T, Calvi P, Wiebe R. Numerical implementation of variable friction sliding base isolators and preliminary experimental results. *Earthq Spectra* 2020;36(2). <https://doi.org/10.1177/8755293019891721>.
- [14] Yang T, Bergquist S, Calvi PM, Wiebe R. Improving seismic performance using adaptive variable friction systems. *Soil Dyn Earthq Eng* 2021;140:106442.
- [15] Monzon EV, Buckle IG, Itani AM. Seismic performance and response of seismically isolated curved steel I-Girder bridge. *J Struct Eng* 2016;142(12). [https://doi.org/10.1061/\(ASCE\)ST.1943-541X.0001594](https://doi.org/10.1061/(ASCE)ST.1943-541X.0001594).
- [16] Mosqueda G, Whittaker AS, Fenves GL, Mahin SA. Experimental and analytical studies of the friction pendulum system for the seismic protection of simple bridges. 2004. Rep. No. EERC 04-01, Earthquake Engineering Research Center, Berkeley, CA.
- [17] Becker TC, Mahin SA. Effect of support rotation on triple friction pendulum bearing behavior. *Earthq Eng Struct Dynam* 2013;42(12):1731–48.
- [18] Darlington RE, Becker TC. Stiffness of rubber bearings considering non-standard top and bottom boundary conditions. *J Struct Eng* 2021;147(7):04021101. 2021.
- [19] Constantinou MC, Whittaker AS, Kalpakidis Y, Fenz DM, Warn GP. Performance of seismic isolation hardware under service and seismic loading. 2007. Technical Report MCEER-07-0012 August 27, 2007.
- [20] Paramashanti KY, Itoh Y, Kitane Y, Gu HS. Long-term performance evaluation of high damping rubber bearings by accelerated thermal oxidation test. 2nd international conference on advances in experimental structural engineering. Shanghai, China: Tongji University; 2007. December 4–6.

- [21] Paramashanti KY, Itoh Y, Kito S, Muratani K. Experimental investigation of aging effect on damping ratio of high damping rubber bearing. *J Struct Eng* 2011;57A: 769–79.
- [22] Higashino M, Hamaguchi H, Minewaki S, Aizawa S. Basic characteristics and durability of low-friction sliding bearings for base isolation. *Earthq Eng Eng Seismol* 2003;4(1):95–105.
- [23] Alvarado AG, Ryan K. Testing and analysis of the effects of contamination of friction pendulum bearings. 2023. Report prepared for Alaska Department of Transportation & Public Facilities.
- [24] Hamaguchi H, Samejima Y, Kani N. A study of aging effect on rubber bearings after about twenty years in use. 11th world conference on seismic isolation, energy dissipation and active vibration control of structures. 2009. Guangzhou, China, November 17–21.
- [25] Van Engelen NC, Kelly JM. Retest of neoprene seismic isolation bearings after 30 years. *Struct Control Health Monit* 2015;22(1):139–51.
- [26] Kato M, Watanabe Y, Yoneda G, Tanimoto E, Hirotani T, Shirahama K, Fukushima Y, Murazumi Y. Investigation of aging effects for laminated rubber bearings of pelham bridge. Proceedings of the 11th world conference on earthquake engineering. 1996. Paper No. 1450, Acapulco, Mexico, June 23–28.
- [27] American Society of Civil Engineers. Minimum design loads for buildings and other structures. 2017. ASCE/SEI 7–16.
- [28] Dao ND, Ryan KL, Sato E, Sasaki T. Predicting the displacement of triple pendulum™ bearings in a full-scale shaking experiment using a three-dimensional element. *Earthq Eng Struct Dynam* 2013;42(11):1677–95.
- [29] Furukawa S, Sato E, Shi Y, Becker TC, Nakashima M. Full-scale shaking table test of a base-isolated medical facility subjected to vertical motions. *Earthq Eng Struct Dynam* 2013;42(13):1931–49.
- [30] Astroza R, Conte JP, Restrepo JI, Ebrahimi H, Hutchinson T. Seismic response analysis and modal identification of a full-scale five-story base-isolated building tested on the NEES@UCSD shake table. *Eng Struct* 2021;238(2021):112087. <https://doi.org/10.1016/j.engstruct.2021.112087>. ISSN 0141-0296.
- [31] Tsai CS, Chiang TC, Chen BJ. Shaking table tests of a full scale steel structure isolated with MFPS. In: Chen JC, editor. Proceedings of the 2003 ASME pressure vessels and piping conference, seismic engineering, 466; 2003. p. 41–7.
- [32] Tsai CS, Chen WS, Chiang TC, Chen BJ. Component and shaking table tests for full-scale multiple friction pendulum system. *Earthq Eng Struct Dynam* 2006;35(11): 1653–75.
- [33] Braga F, Laterza M. Field testing of low-rise base isolated building. *Eng Struct* 2004;26:1599–610.
- [34] He YM, Yang YQ, Dai JW. Field dynamic test for A base-isolated 15-Story steel structure. Proceedings of the 6th international conference on advances in experimental structural engineering and 11th international workshop on advanced smart materials and smart structures technology, August 1–2. Urbana-Champaign, USA: University of Illinois; 2015.
- [35] Wu Y-X, Dong X-J, Lin Y-Q, Cheng H-D. Field test for a base isolation structure on condition of horizontal and initial displacement. *Appl Sci* 2022;12:232. <https://doi.org/10.3390/app12010232>.
- [36] Mazza F. Effects of the long-term behaviour of isolation devices on the seismic response of base-isolated buildings. *Struct Control Health Monit* 2019;e233. <https://doi.org/10.1002/stc.2331>.
- [37] Bolognini D, Dacarro F. Collaudo del Laboratorio Mobile. *Progettazione Sismica* 2018;1.
- [38] Shahnazaryan D, Pinho R, Crowley H, O'Reilly GJ. The built environment data platform for experimental test data in earthquake engineering. *Earthq Eng Struct Dynam* 2024;53(15):4627–40. <https://doi.org/10.1002/eqe.4231>.
- [39] Calvi GM. Mallet-Milne lecture 2025: risk management and rehousing of people displaced by earthquake disasters. *Bull Earthq Eng* 2025;23:2961–3041. <https://doi.org/10.1007/s10518-025-02141-w>. 2025.
- [40] ABAQUS. Analysis user's manual. 2022.
- [41] CEN (Comité Européen de Normalisation). EN 15129: anti-seismic devices. Brussels: CEN; 2009. 2009.
- [42] Ogata A, Aikawa N, Sato M. Design method of low delay FIR bandpass filters. *Proc IEEE Int Symp Circ Syst* 2000;1. I-92–I-95.
- [43] Vandenbussche B, Steyaert M. Multiplicative finite impulse response filters: implementations and applications using field programmable gate arrays. *IET Signal Process* 2015;9(5):419–27.
- [44] Christopoulos C, Filiastrault A. Principles of passive supplemental damping and seismic isolation. IUSS Press; 2006. Istituto Universitario di Studi Superiori di Pavia.
- [45] Fenz DM, Constantinou MC. Development, implementation, and verification of dynamic analysis models for multi-spherical sliding bearings (Report No. MCEER-08-0018). Multidisciplinary Center Earthquake Eng Res 2008. ISSN 1520-295X. Retrieved from, <http://mceer.buffalo.edu/publications/catalog/reports/Development-Implementation-and-Verification-of-Dynamic-Analysis-Models-for-Multi-Spherical-Sliding-Bearings-MCEER-08-0018.html>.
- [46] Rapone A, Calvi PM, Gabbianni G, Becker TC, Sucuoglu H, Chalarca B, Lanese I, Rizzo-Parizi E, Dacarro F, O'Reilly GJ. Dynamic field testing of a 15-Year old base isolated residential building. COMPDYN 2025. In: Papadakakis M, Fragiadakis M, editors. 10th ECCOMAS thematic conference on computational methods in structural dynamics and earthquake engineering. Rhodes Island, Greece, 15–18 June 2025; 2025.
- [47] Calvi GM. L'Aquila earthquake 2009: reconstruction between temporary and definitive. New Zealand society for earthquake engineering inc, 2010 NZSEE conference. 2010. p. 486.
- [48] Ministry of Infrastructure and Transport (MIT). Ministerial decree 14 January 2008: technical standards for construction (NTC 2008) [In Italian: Norme Tecniche per le Costruzioni]. Rome, Italy: Official Gazette of the Italian Republic; 2008. General Series No. 29 of 4 February 2008.
- [49] Priestley MJN, Calvi GM, Kowalsky MJ. Displacement based seismic design of structures. Pavia: IUSS Press; 2007.
- [50] CEN (Comité Européen de Normalisation). EN 1998-1:2004 eurocode 8: design of structures for earthquake resistance – part 1: general rules, seismic actions and rules for buildings. Brussels: CEN; 2004.
- [51] Eroz M, DesRoches R. A comparative assessment of sliding and elastomeric seismic isolation in a typical multi-span bridge. *J Earthq Eng* 2013;17(5):637–57. <https://doi.org/10.1080/13632469.2013.771589>.